



Molecular basis for the calcium-dependent activation of the ribonuclease EndoU

Received: 28 June 2024

Accepted: 24 March 2025

Published online: 01 April 2025

Check for updates

Florian Malard^{1,2}, Kristen Dias³, Margaux Baudy^{1,2}, Stéphane Thore¹, Brune Vialet¹, Philippe Barthélémy¹, Sébastien Fribourg¹, Fedor V. Karginov³ & Sébastien Campagne^{1,2}

Ribonucleases (RNases) are ubiquitous enzymes that process or degrade RNA, essential for cellular functions and immune responses. The EndoU-like superfamily includes endoribonucleases conserved across bacteria, eukaryotes, and certain viruses, with an ancient evolutionary link to the ribonuclease A-like superfamily. Both bacterial EndoU and animal RNase A share a similar fold and function independently of cofactors. In contrast, the eukaryotic EndoU catalytic domain requires divalent metal ions for catalysis, possibly due to an N-terminal extension near the catalytic core. In this study, we use biophysical and computational techniques along with *in vitro* assays to investigate the calcium-dependent activation of human EndoU. We determine the crystal structure of EndoU bound to calcium and find that calcium binding remote from the catalytic triad triggers water-mediated intramolecular signaling and structural changes, activating the enzyme through allostery. Calcium binding involves residues from both the catalytic core and the N-terminal extension, indicating that the N-terminal extension interacts with the catalytic core to modulate activity in response to calcium. Our findings suggest that similar mechanisms may be present across all eukaryotic EndoUs, highlighting a unique evolutionary adaptation that connects endoribonuclease activity to cellular signaling in eukaryotes.

Ribonucleases (RNases) are nucleases that catalyze the processing or degradation of RNA. Found in all organisms, RNases play vital roles in various cellular processes, including the maturation of both coding and non-coding RNAs, combating RNA viruses, and contributing to sophisticated immune strategies like RNA interference^{1–3}. For example, RNases catalyze mRNA decay in general pathways (XRN1, exosome/DIS3L) or as part of apoptotic cascades (RNase L, DIS3L2), carry out unconventional splicing or tRNA cleavage during stress (IRE1, angio-geinin), or catabolize extracellular RNAs (RNase A). Among RNases, the cellular roles of those that cleave endonucleolytically have been increasingly recognized⁴. RNases can be constitutively active (RNase A), or stimulated by ligand binding (RNase L) or cellular signaling

events, such as phosphorylation (IRE1). The ribonuclease A-like domain superfamily (IPRO36816⁵) is the most well-known RNase domain, with many pioneering studies in the 20th century^{6,7}: it was the first directly sequenced enzyme⁸, the first enzyme for which a catalytic mechanism was proposed based on experimental data⁹, and one of the first solved three-dimensional structures¹⁰. Despite its significant impact in enzyme research, it is important to note that the RNaseA-like domain is only found in vertebrates, raising questions about its deeper evolutionary ancestors or relatives⁶.

The endoribonuclease EndoU-like (Endoribonucleases specific for Uridylate) superfamily (IPRO37227⁵) is a poorly understood group of RNases found in bacteria, eukaryotes and viruses. Notably, a structural

¹Univ. Bordeaux, CNRS, INSERM, ARNA, UMR 5320, U1212, Bordeaux, France. ²Univ. Bordeaux, CNRS, INSERM, IECB, US1, UAR 3033, Pessac, France.

³Department of Molecular, Cell and Systems Biology, Institute for Integrative Genome Biology, University of California at Riverside, Riverside, CA, USA.

e-mail: sebastien.fribourg@inserm.fr; fedor.karginov@ucr.edu; sebastien.campagne@inserm.fr

similarity between a bacterial EndoU-like toxin and vertebrate RNase A was identified¹¹. Furthermore, recent studies uncovered an ancient evolutionary link between the Ribonuclease A and EndoU families, suggesting that the animal RNase A gene could have evolved either through significant alteration of an EndoU gene, or by horizontal acquisition of a prokaryotic ribonuclease⁶. XendoU, the founding member of the EndoU-like superfamily (IPRO37227⁵), was initially identified in *Xenopus laevis* oocyte extracts as an enzyme that releases small nucleolar RNAs from introns^{12,13}. In vitro studies demonstrated that XendoU is an endonuclease that cleaves single-stranded RNA with poly(U)-specific activity¹⁴. In eukaryotes, XendoU defines a distinct EndoU family (IPRO18998⁵, PF09412¹⁵) that lacks sequence homology with other known RNases, and is broadly conserved across *Arabidopsis thaliana*, *Drosophila melanogaster*, *Mus musculus*, *Homo sapiens*, and other species^{13,14}. Human EndoU (hEndoU) was first identified as human placental protein 11 (PPI1) due to its prevalence in the placenta¹⁶. In vitro studies have shown that hEndoU cleaves single-stranded RNA preferentially at 5' of uridylates¹⁷. It is also now recognized as a biomarker in various cancers, including squamous cell carcinomas, ovarian adenocarcinomas, non-trophoblastic tumors and breast cancers^{18–22}. In human cells, hEndoU has been proposed to be involved in RNA cleavage, ribonucleoprotein particle removal, and endoplasmic reticulum network organization^{23,24}. Across other eukaryotes, EndoU has been implicated in pro-apoptotic processes in mouse B cells, neuron survival in fruit flies, and synaptic remodeling in nematodes^{25–27}. The more distant bacterial EndoU-like ribonucleases are common in microbial warfare as toxins²⁸.

Members of the EndoU-like superfamily (IPRO37227⁵) exhibit notable differences in their activation requirements. For instance, it is well characterized that EndoU-like bacterial toxins and arteriviral Nsp11 do not need any cofactors for activation, analogous to vertebrate RNase A^{11,29}. In contrast, studies have shown that purified forms of XendoU and coronaviral Nsp15 require millimolar concentrations of divalent calcium or manganese ions^{14,23,30}. The crystal structure of the endoribonuclease XendoU in the absence of divalent metals has been solved³¹, suggesting a catalytic site arrangement similar to that of vertebrate RNase A, specifically featuring a His-His-Lys catalytic triad^{13,31}. However, the structural basis for the metal-dependent activation of eukaryotic EndoUs could not be explained by the crystal structure of XendoU, which represents the inactive state of the endonuclease in the absence of a cofactor³¹. Bacterial and metal independent viral EndoUs share a smaller, C-terminal catalytic domain compared to eukaryotic EndoUs. Because eukaryotic EndoUs contain an N-terminal extension within this catalytic domain that correlates with calcium dependence, we hypothesized that it may bind calcium and control the activity of the catalytic core.

In this study, we elucidated the molecular mechanism of EndoU activation by calcium. First, we established a thymocyte cell line model to confirm the dependence of EndoU on calcium in both cell extract and recombinant forms. Next, we used biophysical methods to detect an allosteric change upon activation by calcium and to solve the structure of active EndoU. Our structural analysis revealed a calcium-stabilized interaction network involving residues from both the eukaryote-specific N-terminal extension and the catalytic core of EndoU, ultimately leading to the activation of the catalytic triad. Our findings provide unprecedented atomic-level insights into a metal ion-activated member of the EndoU-like superfamily (IPRO37227⁵), addressing a longstanding question in the study of eukaryotic EndoUs, which are of significant interest due to their switchable endonuclease activity.

Results

Calcium-dependent RNase activity in mouse thymocyte model

In mammals, EndoU expression is limited to specific cell types. Analysis of Immunological Genome Project data³² on mRNA from 211 mouse

hematopoietic cell types revealed strong mouse EndoU (mEndoU) expression in developing thymocytes, starting at the double negative (DN) 2-3 transition and progressing through the double positive (DP) stages (Fig. 1A). mEndoU expression is absent in the later stages: single positive thymocytes that survive selection and circulating T cells. Outside the hematopoietic system, hEndoU protein staining in human samples showed cytoplasmic expression in stratified squamous epithelia (e.g., skin, esophagus, cervix) and the trophoblast layer in the placenta³³.

For molecular and biochemical analysis of mEndoU, we used the mouse thymic lymphoma cell line VL3-3M2³⁴, which resembles double positive thymocytes with high mEndoU expression (Supplementary Fig. S1A). Upon stimulation with PMA/ionomycin, anti-CD3/CD28, or anti-CD3/CD4, the cell line shows further maturation, including downregulation of Rag1 and mEndoU and upregulation of CD5 (Supplementary Fig. S1B). mEndoU was knocked out in VL3-3M2 cells using CRISPR/Cas9. We confirmed the deletion of the genomic region (Supplementary Fig. S1C) and the loss of mEndoU mRNA (Supplementary Fig. S1D). We assayed endogenous ribonuclease activity in WT and mEndoU KO VL3-3M2 extracts, based on experiments performed in *Xenopus laevis* egg extracts²³. Incubation of cytoplasmic extracts at 37 °C for 15 min without divalent metals caused no RNA degradation (Fig. 1B). However, WT extracts supplemented with 5 mM calcium showed robust RNA cleavage, which was absent in mEndoU KO extracts and rescued by expressing WT or HA-tagged mEndoU in KO cells (Fig. 1B). Thus, VL3-3M2 extracts have a strong calcium-dependent ribonuclease activity, which can be attributed to mEndoU.

To confirm the role and enzymatic properties of mEndoU, we used HA-tagged mEndoU rescue cells for on-bead in vitro cleavage assays with immunoprecipitated mEndoU. Since mEndoU cleaved various RNA sequences (Supplementary Fig. S2A), we used an arbitrary substrate (50 mer 1) for subsequent experiments (Supplementary Table S2). Time course measurements (Fig. 1C, Supplementary S1B) were used to calculate initial reaction rates (Supplementary Fig. S2C). Based on previous studies¹⁷, the mutation of two critical residues in mEndoU (E285A/H286A) abolished its enzymatic activity (Fig. 1D), confirming the role of mEndoU in RNA cleavage. We showed that only calcium stimulated cleavage, unlike manganese or other divalent metals (Fig. 1E, Supplementary S2B), with optimal activity at 1–2 mM calcium. mEndoU showed little dependence on Na⁺ or K⁺ and sustained activity across pH 4–8 (Supplementary Fig. S2D–F). These results indicate mEndoU is a calcium-activated ribonuclease targeting a large repertoire of RNAs.

Structural basis for hEndoU activation by calcium ions

To examine structural changes in hEndoU upon calcium activation, we first computed a homology model of apo-hEndoU using apo-XendoU crystal structure³¹ as template via SWISSMODEL³⁵. The modeled apo-hEndoU structure is globular, with a predominantly β-sheet catalytic core and an α-helical bundle N-terminal extension (Supplementary Fig. S3A). We expressed the XendoU catalytic domain (Fig. 1F) of hEndoU (I35–410) with ¹⁵N labeling for NMR spectroscopy. In the ¹⁵N SOFAST-HMQC spectrum of apo-hEndoU, we observed well-dispersed but broader, and fewer signals than expected, suggesting conformational exchange in the μs-ms range (Supplementary Fig. S3B). Accordingly, we could not record suitable triple-resonance NMR experiments to reliably assign the backbone of apo-hEndoU. Size Exclusion Chromatography with Small-Angle X-ray Scattering (SEC-SAXS) confirmed that the folding of recombinant hEndoU is consistent with theoretical predictions (Supplementary Fig. S3C). Furthermore, the crysol program³⁶ showed strong correlation between experimental and theoretical SAXS data, validating the structural model (Supplementary Fig. S3D).

We then studied the effect of divalent metal ions on hEndoU structure and dynamics by comparing ¹⁵N SOFAST-HMQC spectra of

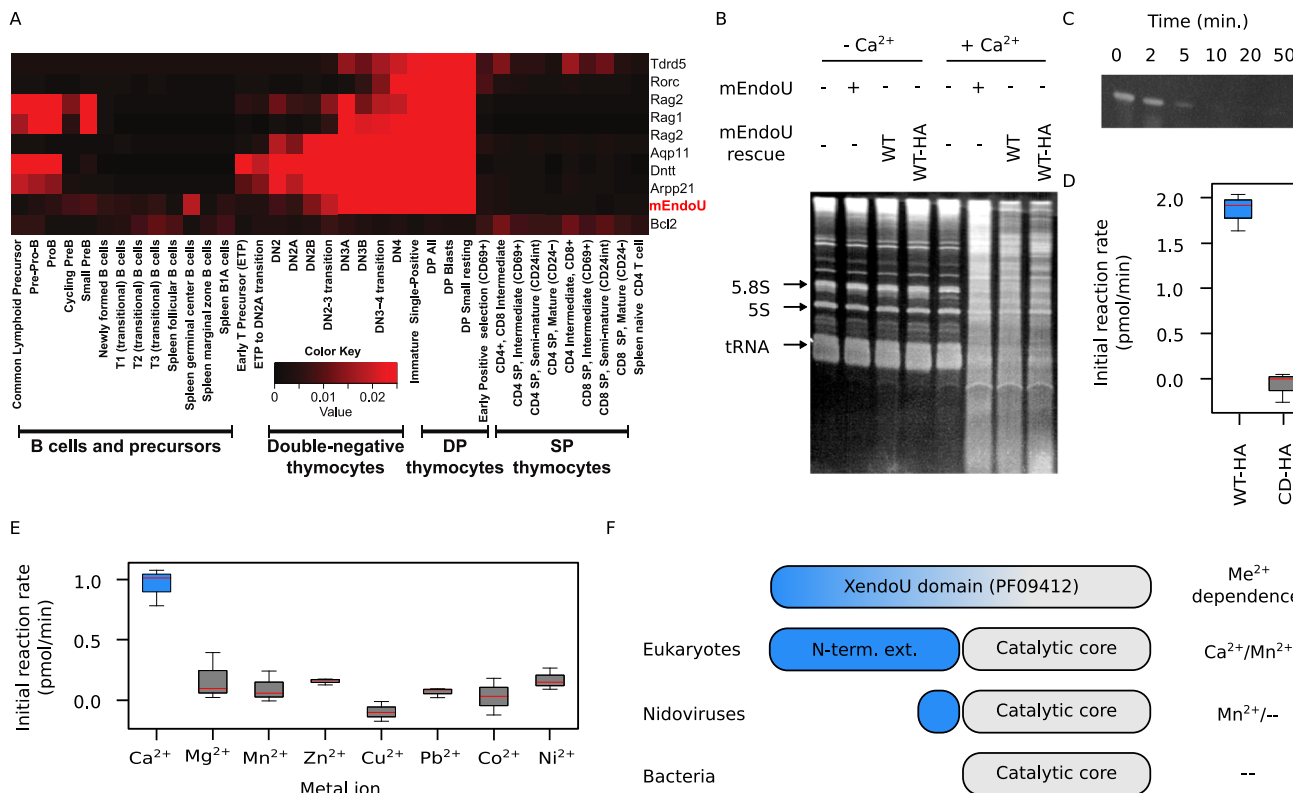


Fig. 1 | mEndoU is expressed during thymocyte development and has a calcium-activated RNase activity. A mEndoU expression levels in developing thymocyte populations. The color indicates fractional expression of the mRNA across 211 measured cell types. Data from the Immunological Genome Project³². B RNase activity in WT and mEndoU KO cell lysates. Cytoplasmic lysates from the indicated WT, KO or rescue cell lines were incubated +/− 5 mM calcium for 15 min at 37°C. RNA was extracted, 5 µg were run on an 8 % urea-PAGE gel, and visualized by SYBR Green II. WT-HA denotes a WT mEndoU rescue construct with a C-terminal HA tag. C Immunoprecipitated mEndoU cleavage activity on a defined RNA substrate. D Cleavage activity of WT mEndoU (WT-HA) and the catalytically dead (CD-HA) mEndoU double mutant E285A/H286A. The initial reaction rate was significantly higher for WT-HA compared to CD-HA ($p = 0.0002$). E mEndoU RNase activity is specifically activated by calcium ions. The initial reaction rate was significantly higher for calcium compared to Mg^{2+} ($p = 0.02$), Mn^{2+} ($p = 0.01$), Zn^{2+} ($p = 0.01$), Cu^{2+} ($p = 0.01$), Pb^{2+} ($p = 0.01$), Co^{2+} ($p = 0.01$), and Ni^{2+} ($p = 0.01$). For (D) and (E),

experiments were done in triplicate. Initial reaction rates were computed from linear regression at early time points for each replicate and they are plotted as boxplot, with the center line representing the median, the box bounds indicating the 25–75th percentiles, and the whiskers extending to the minimum and maximum values. Checks for normality and equal variance across the data were performed using the Shapiro-Wilk and Levene's tests, respectively. Group comparisons were achieved with pairwise independent two-sample, one-sided t-tests. The p -values were adjusted using the Benjamini-Hochberg method for multiple testing correction. Source data are provided as a Source Data file. F Topology of XendoU domains across phyla. The XendoU domain (PF09412³⁵) consists of a C-terminal catalytic core that is conserved across phyla. It features a long N-terminal extension specific to eukaryotes and a short N-terminal extension specific to nidoviruses. In eukaryotes, the presence of the N-terminal extension correlates with a dependence on metal ions.

apo-hEndoU to metal-bound states. Saturating concentrations of magnesium, nickel, or strontium caused signal loss in the NMR spectra, suggesting either protein aggregation or increased conformational exchange (Supplementary Fig. S4A–C). In contrast, saturating calcium restored a set of well-dispersed peaks in the NMR spectrum (Supplementary Fig. S4D). At sub-saturating calcium levels, we observed chemical shift perturbations and a shift in the fluorescence spectrum of the protein (Supplementary Fig. S5A, B). Intriguingly, the addition of a 2'-fluorinated (2'-F) nonhydrolyzable RNA in the presence of sub-saturating calcium produced effects similar to those observed with saturating calcium, including the restoration of a set of well-dispersed peaks (Supplementary Fig. S5C). This was not observed in the absence of calcium, where the substrate analog did not significantly alter the NMR spectrum (Supplementary Fig. S5D). These findings suggest a two-step activation process involving local structural changes at lower calcium concentrations and the abrogation of conformational exchange in the μ s-ms range at higher calcium concentrations or upon binding of a substrate analog.

To elucidate the effect of calcium, we crystallized hEndoU with an excess of calcium and solved its structure at 1.7 Å resolution. The

structure revealed five calcium ions, with one aiding crystal packing and four potentially activating the protein (Fig. 2A, Supplementary Fig. S6). Each calcium ion is coordinated by seven oxygen atoms from acidic side-chains, backbone carbonyl groups, or protein-stabilized water molecules (Fig. 2B). Sites (1) and (3) include residues from both the catalytic core and the eukaryote-specific N-terminal extension (Fig. S7), with site (1) located 12.8 Å away from the catalytic triad (H285, H300, K343). Comparing apo-hEndoU homology model and calcium-activated hEndoU structure revealed conformational changes upon calcium binding that primarily cluster in protein loops near the catalytic triad (Fig. 2C, D). The side-chain of E290, located midway between site (1) and the catalytic triad, flips to engage with a water molecule in the calcium coordination network. This correlates with the side-chain rotation of catalytic H285, then locked by an electrostatic interaction with E290 (Fig. 2C). In apo-hEndoU, the loop containing E290 does not have a defined secondary structure, and calcium binding correlates with the formation of a β-hairpin in the vicinity of the catalytic site (Fig. 2D). Our data show a model for the calcium-dependent regulation of hEndoU through allostery, with site (1) and residue E290 as key mediators in the intramolecular signaling leading to hEndoU activation.

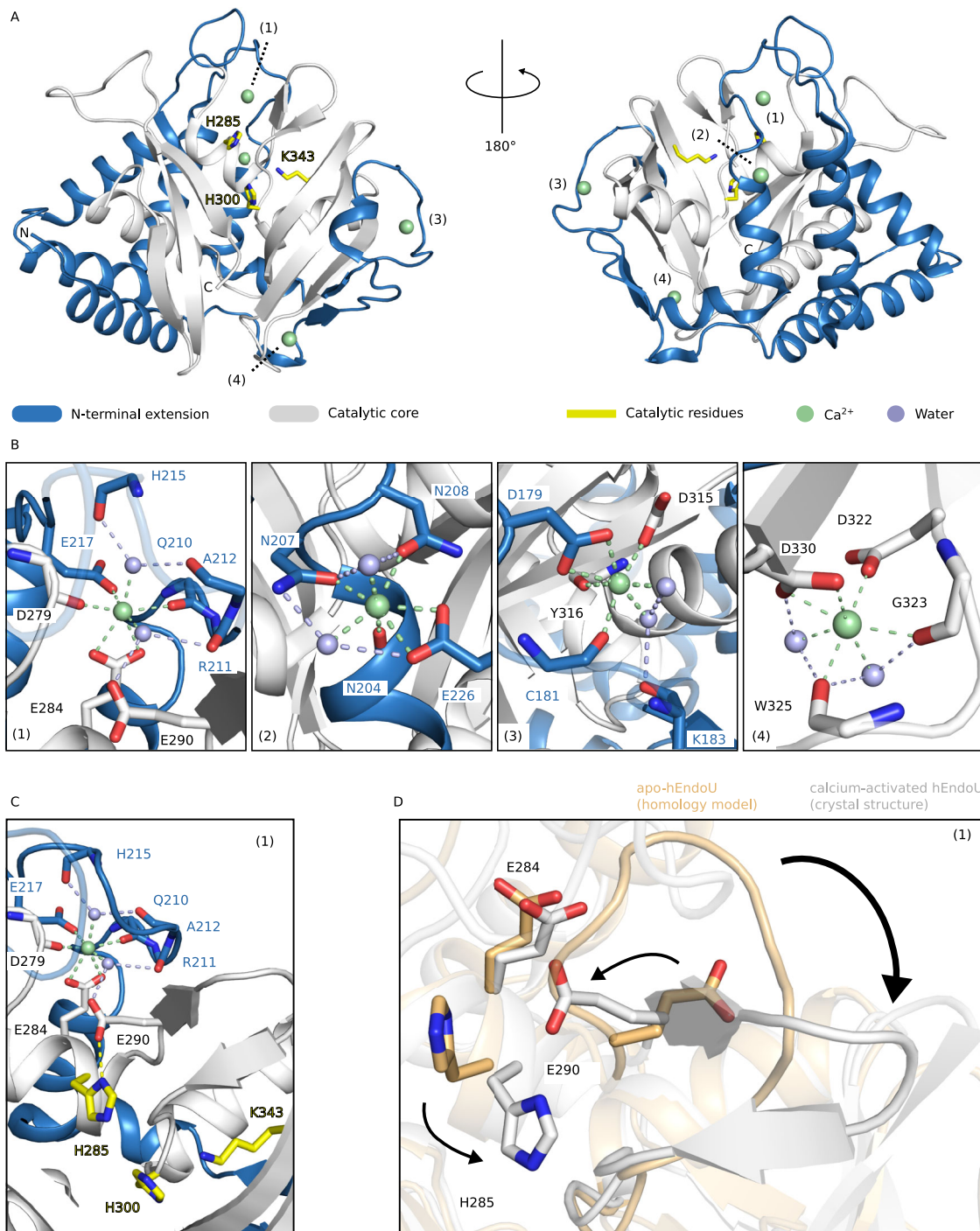


Fig. 2 | Crystal structure of calcium-activated hEndoU. **A** Overview of calcium-activated hEndoU structure. Calcium binding sites (1)–(4) as referred in the text are indicated. **B** Closeup view of hEndoU calcium binding sites. Residues from the catalytic core (white) and from the N-terminal extension (blue) are highlighted. **C** Intramolecular signaling between calcium binding site (1) and remote catalytic

residues. Catalytic residue (yellow) are highlighted, along with residues from the catalytic core (white) and from the N-terminal extension (blue). **D** Structural change upon hEndoU allosteric activation by calcium. For **(A–D)**, the calcium-binding sites are labeled with numbers in parentheses (black).

Experimental validation of hEndoU activation model

To validate our structure-based model for calcium-mediated hEndoU activation, we first designed mutants with altered calcium-binding sites. RNA degradation assays were conducted for each variant (Fig. 3A). Without calcium or wild-type hEndoU, no RNA cleavage was detected, whereas their presence led to almost complete RNA degradation over time. The degradation data fitted a first-order reaction model, providing a kinetic parameter describing the reaction (Fig. 3B).

Disrupting calcium binding sites (2) or (4) with mutations E226A or D330A led to RNA degradation rates similar to the wild-type (Fig. 3A, C). In contrast, disruption of calcium binding sites (1) or (3) with mutations E284A or D179A abolished enzymatic activity. Interestingly, calcium binding sites (1) and (3) are defined by residues from both the catalytic core and the eukaryote-specific N-terminal extension, while this is not the case for sites (2) and (4) (Supplementary Fig. S7). Moreover, the side chains of residues E217 and E284 directly

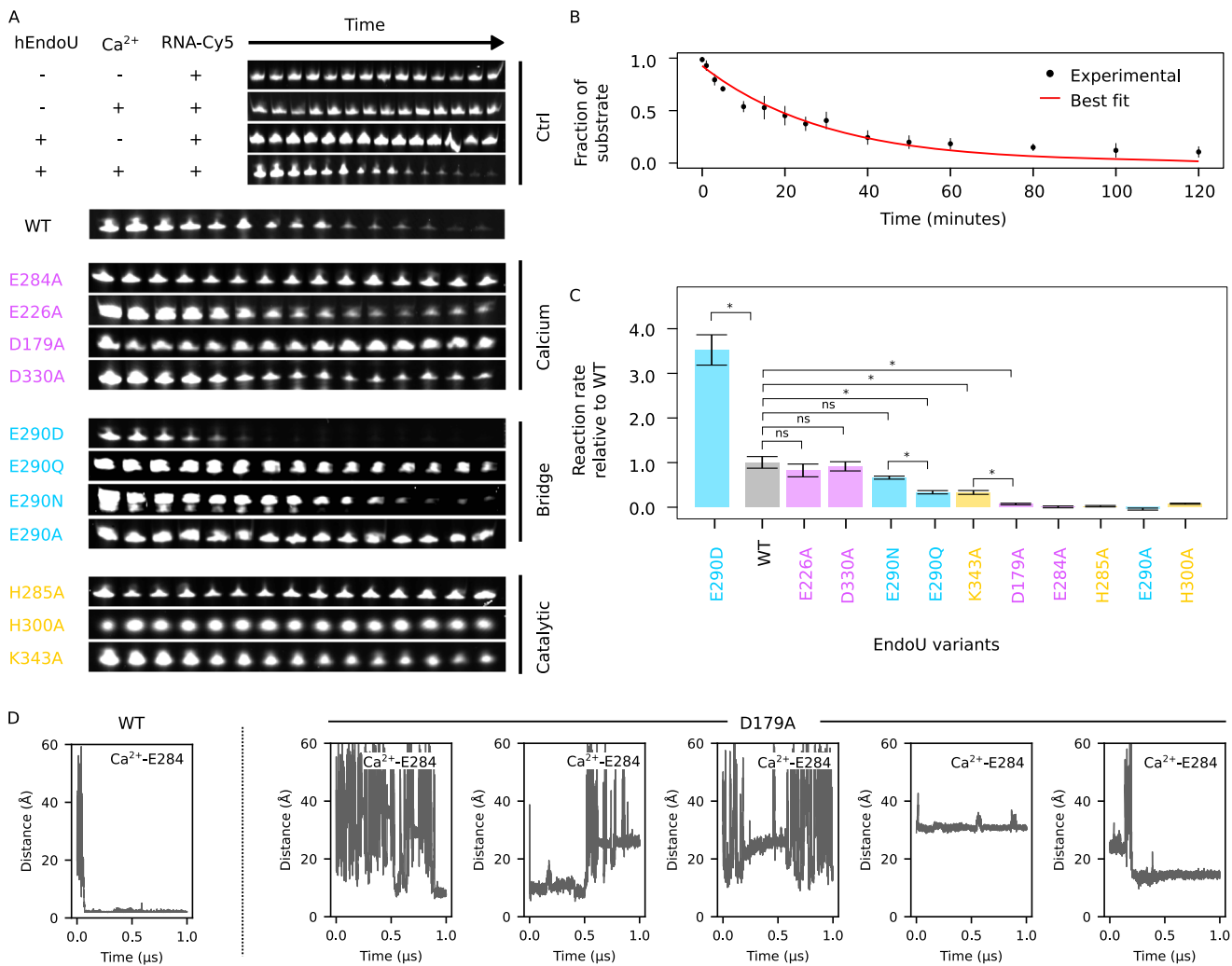


Fig. 3 | Enzymatic activity of hEndoU and its mutants. A RNA degradation assays. Comparison of mutants for calcium-binding sites (magenta), the bridging residue E290 (cyan), and catalytic residues (yellow) with wild-type hEndoU over a 2 hrs degradation assay. The RNA was labelled with Cy5 at the 3' end, with the sequence 5'-CAGGUUUCCCCAACGAAAAAAAAA-3'. Experiments were done in triplicate. **B** Enzymatic progress curve. Example of fit for a first-order reaction model $A \times \exp(-k \times t)$ with wild-type hEndoU. Across replicates, the mean fraction of substrate at each time point (plotted value) and the standard deviation (error bars) are shown. **C** Relative reaction rates of hEndoU mutants compared to wild-type. The fitted reaction rate is expressed relative to the wild-type (plotted value), and the error in the fitted reaction rate was propagated to be expressed consistently (error

bars). Statistical significance was assessed by computing a z-score for the difference between each pair of reaction rates, adjusting for their respective errors, and then these z-scores were converted into two-tailed *p*-values adjusted for multiple comparisons using Bonferroni correction. Statistical significance (*p*<0.05) and non-significance (ns) are highlighted for a representative set of pairwise comparisons. For **(B)** and **(C)**, experiments were done in triplicate and source data are provided as a Source Data file. **D** Calcium binding to hEndoU WT or D179A monitored through Molecular Dynamics. Each plot displays the distance between the E284 side-chain carboxylate and a calcium ion throughout the simulation. Five calcium ions were introduced in the simulation box.

contribute to calcium coordination at site (1), as do D179 and D315 at site (3) (Supplementary Fig. S8). All show identity conservation, with the exception of D315, which can present a semi-conservative substitution to asparagine across eukaryotic EndoUs (Supplementary Fig. S8).

Our results clearly indicate that the eukaryote-specific N-terminal extension of hEndoU contributes to calcium sensing, thereby enabling allosteric regulation. Even though the crystal structure of calcium-activated hEndoU could explain the role of calcium binding site (1) in this process, it was not the case for site (3). We hypothesized that calcium binding to site (1) could be promoted by a prior binding event at site (3) and relied on Molecular Dynamics (MD) experiments to test this hypothesis. With the wild-type hEndoU, we observed calcium binding to site (1) within less than 100 ns simulation time (Fig. 3D). Disrupting site (3) with mutation D179A resulted in no stable binding at site (1) for any of the five calcium ions added in the 1 μ s simulation. This

suggests that an interplay between calcium binding sites (1) and (3) might lead to hEndoU activation, through a yet undetermined mechanism.

We further proposed that calcium sensing at site (1) was communicated to the remote catalytic site through water-mediated intramolecular signaling events enabled by key residue E290 (Fig. 2C). Disruption of the intramolecular signaling cascade by mutation E290A completely abolished enzymatic activity while preserving calcium binding (Supplementary Fig. S9A), thereby fully uncoupling calcium binding from catalytic activation, whereas the semi-conservative E290Q mutation partially uncoupled these events, reducing enzymatic activity to about half that of the wild type (Fig. 3A, C). Assessing side-chain length revealed that the charge-conservative E290D mutation increased enzymatic rate 4-fold, while E290N nearly doubled the activity of E290Q and matched wild-type levels, collectively indicating that, in addition to polarity as primary

factor, shorter side-chains enhance enzymatic activity (Fig. 3A, C). Consistent with our structural model, a negatively charged sidechain at position 290 is optimal for the allosteric activation of hEndoU by calcium. In this model, E290 locks the catalytic H285 side-chain in an active conformation. Accordingly, substitution of catalytic H285 with alanine completely abrogated enzymatic activity, as observed for catalytic mutant H300A, underscoring the importance of the histidine pair in catalysis. Substitution of catalytic residue K343 by alanine resulted in a reduction to nearly half of the enzymatic activity, consistent with the role of K343 as a stabilizer of reaction intermediates. Overall, mutagenesis experiments corroborate the residue assignments proposed in our structure-based model for calcium-mediated activation of hEndoU.

Calcium-activated hEndoU in complex with RNA

We established that calcium activates hEndoU by triggering an allosteric network that remotely activates the catalytic triad. Without calcium, binding of 2'-F RNA showed limited impact on the ^{15}N SOFAST-HMQC spectrum of hEndoU (Supplementary Fig. S5D). Repeating the experiment with a phosphodiester RNA yielded similar results, indicating a weak interaction in the absence of calcium (Supplementary Fig. S10A). Consistent with our calcium-dependent activation model, this weak binding did not lead to RNA degradation (Figs. 2 and 3). To assess the impact of calcium on RNA binding, we used Electrophoretic Mobility Shift Assay (EMSA) with the catalytically dead hEndoU mutant H285A, which still binds calcium, and a phosphodiester RNA containing a single uridylate (Supplementary Figs. S9B and S11A). Without calcium, EMSA did not detect the weak interaction observed by NMR, likely due to its inability to detect complexes with fast dissociation rates. However, increased calcium concentrations strongly populated a low molecular weight (LMW) complex and a weakly populated high molecular weight (HMW) complex (Supplementary Fig. S11A). A control experiment, in which the single uridylate was replaced by another nucleotide, resulted in a significant increase in free RNA and a weakly populated LMW complex (Supplementary Fig. S11B). Interestingly, we observed calcium-dependent RNA binding to the hEndoU E284A mutant, despite its lack of catalytic activity (Supplementary Fig. S11C, 3A, C). This indicates that enzyme activation does not result from the calcium-dependent enhancement of hEndoU interaction with RNA, consistent with our model (Fig. 2C). Altogether, we conclude that calcium promotes the formation of an uridylate-specific complex, but also of higher order complexes due to non-specific secondary binding to other nucleotides.

To experimentally determine the RNA-binding surface of calcium-activated hEndoU, we first recorded triple resonance NMR experiments for backbone chemical shift assignment of calcium activated hEndoU, successfully assigning 89.3% (251 out of 281 residues) of the backbone resonances³⁷ (Supplementary Fig. S12). Excluding the N-terminal GGSEFA sequence and nine proline residues, the assignment coverage increased to 94.3 %. Next, we recorded ^{15}N and ^{13}C SOFAST-HMQC spectra of calcium-activated $^{13}\text{C}^{15}\text{N}$ -labeled hEndoU with a 2'-F RNA substrate analog (Supplementary Fig. S13A, B). Severe line broadening in a subset of crosspeaks and additional spectral changes in the rapid exchange regime were observed (Supplementary Fig. S13A). We calculated ^1H - ^{15}N chemical shift perturbations between calcium-activated hEndoU and upon RNA binding, noting particularly the residues that disappeared in the bound state (Fig. 4A). All disappearing residues are located in the C-terminal catalytic core, covering the β -sheet surface composed of two independent β -sheets and a short α -helix (Fig. 4B). The strongest chemical shift perturbations also correspond to residues in this area. Electrostatic analysis indicated that the β -sheet is highly basic, suitable for RNA binding (Fig. 4C). In contrast, the N-terminal α -helical region showed minimal changes upon RNA binding, with no disappearing resonances, and displayed a neutral or acidic surface

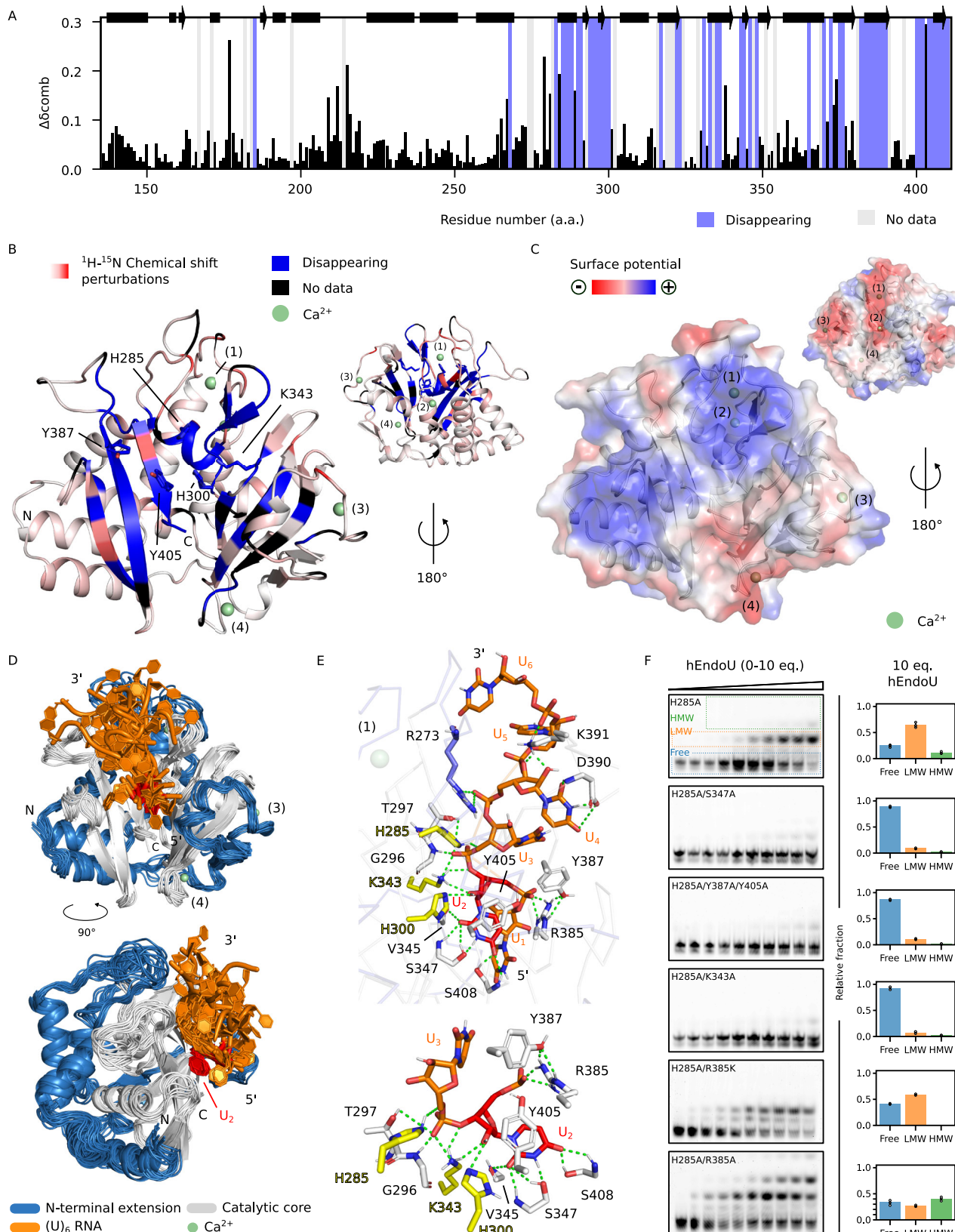
charge. These data support that RNA binds to the conserved catalytic core of the protein, involving an extended, basic β -sheet-rich groove.

To model the complex between calcium-activated hEndoU and RNA, we used AlphaFold (AF) 3³⁸ with the primary sequence of hEndoU, a (U)6 RNA, and four calcium ions as inputs. We controlled that a 2'-F (U)6 RNA analog interacts with calcium-activated hEndoU (Supplementary Fig. S10B). We then conducted a 1 μs Molecular Dynamics (MD) simulation using the top-ranked AF model to prepare the input. Over the trajectory, we clustered structures based on RNA conformations to obtain a final ensemble of RNA-bound calcium-activated hEndoU models (Fig. 4D). All models consistently reproduced the crystal structure of calcium-activated hEndoU, with a mean RMSD of $1.18 \pm 0.29 \text{ \AA}$. The intermolecular interface with the (U)6 RNA is defined by the cleft between the two front β -sheets, where nucleotide U2 anchors in close proximity to the catalytic triad, exposing its sugar 2'-OH for nucleophilic attack by residue H300 (Fig. 4E, Supplementary Fig. S14). Conformational heterogeneity is observed at the interface with hEndoU across the models for the rest of the RNA sequence, in agreement with the experimental NMR data showing line broadening for residues in the RNA-binding region due to conformational sampling in the μs -ms range. Overall, the ensemble of models aligns well with our experimental data, providing a robust structural hypothesis for calcium-activated, RNA-bound hEndoU.

To further validate our ensemble of models, we conducted mutagenesis experiments targeting residues interacting with U2 near the active site (Fig. 4E, Supplementary Figs. S14, S15), which showed consistent contacts across models with an RMSD of $0.73 \pm 0.35 \text{ \AA}$ (Fig. 4D, E). We selected K343, S347, R385, Y387, and Y405, and generated mutants in the catalytically dead hEndoU H285A background (Fig. 2A, C), evaluating RNA binding via EMSA in the presence of calcium (Fig. 4F). The hEndoU H285A mutant showed consistent RNA binding, with a stoichiometric complex corresponding to uridylate-specific binding, and higher order complexes corresponding to non-specific secondary binding. Mutations S347A and K343A were expected to disrupt electrostatic interactions with U2, reducing RNA binding. In agreement with our model, double mutants H285A/S347A and H285A/K343A showed dramatically reduced RNA binding. Similarly, the triple mutant H285A/Y387A/Y405A exhibited weak RNA binding, possibly resulting from the loss of π -stacking between Y405 and U2 and destabilization of R385 conformation due to the absence of the Y387 hydroxyl group (Fig. 4E). The conservative mutation R385K (H285A/R385K) had limited impact on RNA binding. Unexpectedly, the double mutant H285A/R385A, which should reduce RNA binding, showed increased secondary binding at high protein:RNA ratios, suggesting enhanced binding to non-uridylate bases. Our findings demonstrate that specific residues at the hEndoU-RNA interface are essential for substrate binding, providing further experimental evidence supporting our AI/MD-derived model.

Discussion

In this work, we elucidated the molecular basis of calcium-dependent hEndoU activation, a mechanism likely conserved across eukaryotic EndoUs due to their highly conserved catalytic domain. Although we unveiled the molecular basis for the calcium-dependent activation of hEndoU, it should be noted that we did not establish the molecular basis explaining the specificity of hEndoU activation by calcium ions. Nevertheless, our findings indicate that calcium induces allosteric activation rather than directly participating in catalysis (Fig. 5A). A metal-independent catalytic mechanism supports the proposed common evolutionary origin of EndoU-like domains and the RNase A family, as suggested by structural and distant sequence similarities⁶. Both EndoU and RNase A produce a 5'-OH product characteristic of metal-independent endonucleolytic catalysis³⁹, and EndoU-like toxins as well as certain viral EndoUs function without divalent metal ions^{11,29}.



The endonucleolytic activity of RNase A and EndoU-like domains relies on a conserved catalytic triad composed of two histidines and one lysine^{13,40} (Fig. 5B, Supplementary Fig. S8). Of note, the crystal structure of XendoU bound to a phosphate ion suggests that residues H162 and H272 could define the catalytic site³¹ (Fig. 5B). However, H272 in XendoU is not conserved, and other studies have proposed the universally

conserved H162 and H178 instead¹³, in line with our findings of catalytic H285 and H300 in hEndoU. In terms of spatial arrangement, the catalytic residues H12 and K41 in RNase A align well with corresponding residues in EndoU-related proteins, whereas residue H119 is spatially shifted (Supplementary Fig. S16). The closest spatial equivalent to H119 in RNase A is H187 in a bacterial EndoU-like toxin, while H285 in

Fig. 4 | Experimental characterization and modeling of calcium-activated hEndoU in complex with RNA. **A** Combined ^1H - ^{15}N chemical shift perturbations between calcium-activated ^{13}C - ^1H -hEndoU and in complex with 2'-F RNA. Source data are provided as a Source Data file. **B** RNA binding interface mapping on calcium-activated hEndoU. **C** Electrostatic surface potential of calcium-activated hEndoU. **D** Structure alignment of the ensemble of models ($N=14$) for calcium-activated hEndoU in complex with RNA. The alignment was performed on the protein region. **E** Detailed view of a representative model of the ensemble with

highlight on protein-RNA interactions. A close-up view of interactions at U2-U3 is also shown. **F** RNA binding to calcium-activated hEndoU mutants monitored by EMSA. The regions corresponding to the free Cy5-labeled RNA, the low molecular weight complex (LMW), and the higher molecular weight complexes (HMW), are highlighted. Experiments were done in triplicate. For each experiment, the relative fraction of Free RNA, LMW, and HMW complexes were computed for each replicate, and the resulting means (plotted values) and standard deviations (error bars) were plotted at 10 eq. hEndoU.

hEndoU and H234 in Nsp15 are more distantly located. This spatial rearrangement likely reflects evolutionary divergence while preserving a metal-independent catalytic mechanism.

On the other hand, we demonstrated that calcium binding activates hEndoU through allostery, and we propose that this mechanism might be conserved across all eukaryotic EndoUs. Indeed, we identified calcium binding sites (1) and (3) as critical for hEndoU activation, and they are highly conserved in eukaryotic EndoUs, supporting a shared activation mechanism (Supplementary Fig. S8). In addition, we have shown that calcium-coordinating residues at these sites originate from both the conserved catalytic core and the eukaryote-specific N-terminal extension. Although not essential for activation, site (2) is also broadly conserved, suggesting a putative function awaiting characterization. In contrast, site (4) is poorly conserved, consistent with its nonessential role for activation. Future studies will aim to understand the function of calcium binding site (3), as our data suggest an interplay with site (1). Nevertheless, we have shown that calcium binding to site (1) triggers an allosteric network responsible for structural rearrangements and the activation of the remote catalytic residues. Overall, we have established that calcium does not directly participate in catalysis but instead allosterically activates the catalytic triad, with the eukaryote-specific N-terminal extension acting as a calcium sensor, a model that we believe is relevant to all eukaryotic EndoUs. We have shown that eukaryotic mEndoU and hEndoU are specifically activated by calcium, consistently with previous studies²³. Although early work on *Xenopus* suggested a manganese requirement, calcium-dependent cleavage was also observed¹². Similarly, the *C. elegans* endu-2 is activated by both calcium and manganese⁴¹. However, the physiological relevance of manganese activation in mammals remains unclear due to low manganese levels in tissues⁴². In contrast, calcium concentrations vary widely, making the localization of EndoU crucial for the significance of calcium-dependent activation. Interestingly, animal EndoUs often feature signal peptides and sometimes somatomedin B (SmB) domains rich in disulfide bonds, suggesting secretion or ER association^{43–45}. Indeed, some EndoUs are secreted and can be reuptaken, while others are cytoplasmic and ER-associated^{23,44,46}. Given that cellular calcium levels rise substantially during signaling events⁴⁷, EndoU could cleave RNA or modulate mRNA expression in processes such as thymocyte maturation or apoptosis, aligning with its proposed pro-apoptotic function in B cells²⁵. Although the calcium activation mechanism might be conserved across eukaryotic EndoUs, species-specific localization and RNA targets can vary. If delivered to calcium-rich extracellular environments, EndoU could degrade extracellular RNA, underscoring the importance of understanding its RNA-targeting repertoire to further elucidate its biological roles.

Nonetheless, our results also indicate that calcium promotes hEndoU binding to RNA independently of enzymatic activation. Interestingly, SARS-CoV-2 Nsp15, which contains a nidovirus EndoU-like domain (NendoU), requires divalent manganese ions to cleave the 5'-polyuridine tract of its negative-sense RNA⁴⁸. However, the conserved metal-coordination sites found in eukaryotic EndoUs are absent in Nsp15 and related viral homologs (Supplementary Fig. S8), suggesting that manganese might enhance enzymatic activity by promoting Nsp15-RNA interaction, mirroring the observed effect of calcium in promoting hEndoU binding to RNA. Consistently, recent *in vitro* studies demonstrated that Nsp15 retains some activity on

single-stranded RNA without divalent metal ions, although manganese increases this activity in a substrate-dependent manner^{49,50}. Other reports also found enhanced RNA binding by Nsp15 in the presence of manganese⁵¹ and suggest that manganese may provide charge shielding to promote Nsp15 interactions with the RNA⁵², although it has also been proposed that manganese stabilizes an alternative enzymatic state with a higher cleavage rate⁴⁹. Insights from Nsp15 studies also highlight the significance of tipiracil, a uridine analog that binds the Nsp15 uridine binding site and inhibits its activity⁵³. Determining whether tipiracil can similarly bind and inhibit eukaryotic EndoUs would provide a valuable tool for probing their cellular and extracellular functions.

Finally, recent studies describing Nsp15 structures through the whole RNA cleavage process⁵² uncovered uridine-specific interactions involving a conserved serine residue. In our model of calcium-activated hEndoU in complex with a (U)₆ RNA, the corresponding S347 residue also maintains uridine-specific hydrogen bonds, suggesting a degree of conservation in uridine recognition across phyla. However, there is a discrepancy regarding the cleavage site in EndoU enzymes. Some reports indicate that Nsp15 can cleave at the 5' side of uridylate^{30,54}, as also proposed for hEndoU¹⁷. Nevertheless, structural evidence from Nsp15 clearly indicates cleavage on the 3' side of uridylate⁵². Our model for calcium-activated hEndoU also supports cleavage on the 3' side of uridylate, consistent with Nsp15⁵², the bacterial EndoU-like toxin MafB⁵⁵, and RNase A⁷. Therefore, further structural and biochemical studies are required to unambiguously determine on which side of uridylates eukaryotic EndoU members achieve cleavage.

In conclusion, we have determined the molecular basis for the calcium-dependent activation of hEndoU, revealing a crucial role for the eukaryote-specific N-terminal extension and proposing a conserved allosteric activation mechanism across eukaryotic EndoUs. Our findings pave the way for further studies that explore eukaryotic EndoUs within the broader EndoU-like superfamily (IPRO37227⁵), aiming for a better understanding of these metal-ion-responsive ribonucleases.

Methods

Cell culture

VL3-3M2 mouse thymic lymphoma cells³⁴ (obtained from Stephen Smale's lab, UCLA) were cultured in RPMI 1640 (Corning) supplemented with 10 mM HEPES, 50 μM β -mercaptoethanol, 1× penicillin/streptomycin, and 10% fetal bovine serum (FBS). The Platinum-E (Plat-E) retroviral packaging cell line (Cell Biolabs, RV-101) was cultured in DMEM (Corning) supplemented with 10 % FBS (Corning) and 10 units/mL of penicillin/streptomycin (Gibco). All cells were grown at 37 °C in an atmosphere containing 5% CO₂, and were regularly tested negative for mycoplasma contamination.

VL3-3M2 TCR activation

Cell culture 6-well plates were pre-incubated overnight at 37 °C with 1 mL of PBS, either with or without 5 $\mu\text{g}/\text{mL}$ of anti-CD3e/CD28 (BD Pharmingen, clone 145-2C11, #553057; BD Pharmingen, clone 37.51, #553295) or anti-CD3/CD4 antibodies (BD Pharmingen, clone 145-2C11, #553057; BD Pharmingen, rat anti-mouse CD4, clone GK1.5, #553726). The PBS was then aspirated, and 5 \times 10⁵ cells in 2 mL of media were

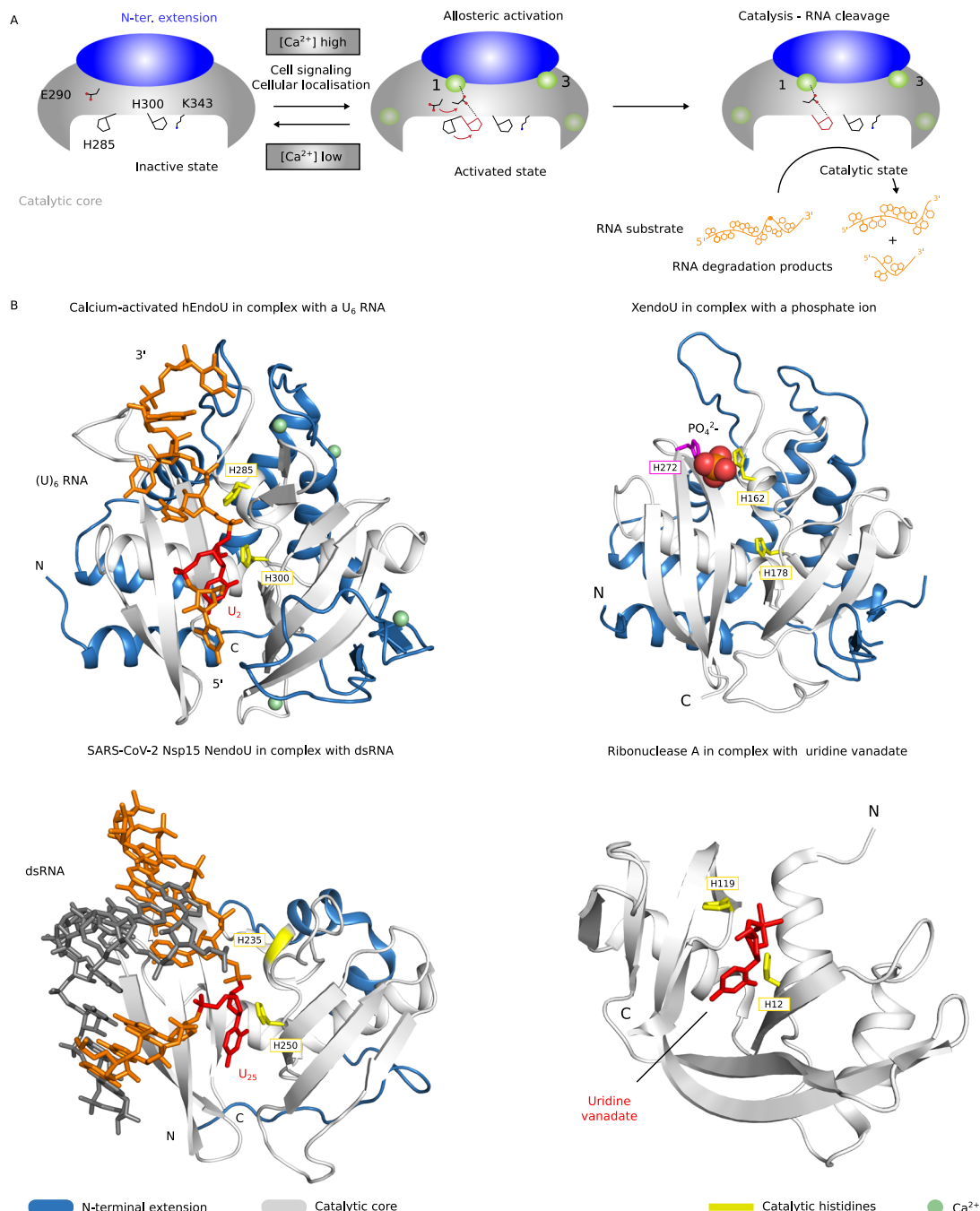


Fig. 5 | Summary of eukaryotic EndoU activation and structure comparison with homologs. **A** Schematic representation of eukaryotic EndoU activation upon calcium and substrate binding. **B** A representative model of calcium-activated, RNA-bound hEndoU is shown alongside the crystal structure of apo-XendoU bound to a phosphate ion (PDB: 2C1W), the cryo-EM structure of SARS-CoV-2 Nsp15 NendoU in complex with dsRNA (PDB: 7TJ2), and the liquid-state structure of ribonuclease A in complex with uridine vanadate (PDB: 6RSA). For each model or

structure, the catalytic histidines are highlighted (yellow). For the crystal structure of apo-XendoU, the residue H272, which was assigned as part of a phosphate binding site in a previous study³¹, is highlighted (magenta). For hEndoU, XendoU, and Nsp15, the N-terminal extension upstream of the catalytic core is highlighted (skyblue). For the model of calcium-activated, RNA-bound hEndoU, calcium ions are shown (palegreen).

added. For PMA/ionomycin stimulation, concentrations of 20 ng/mL and 500 ng/mL were used, respectively. Total RNA was extracted using Trizol 24 h later, and RT-qPCR measurements were conducted for EndoU, Rag1, and CD5, normalized against a β-actin control. Fold changes were calculated relative to an unstimulated control.

mEndoU knockout cell generation

mEndoU KO VL3-3M2 cells were generated as previously described⁵⁶. sgRNAs designed to target intron 1 and exon 11 of the mEndoU locus

(Supplementary Table S1) were cloned into the pSpCas9(BB)/pX330 Cas9-sgRNA expression plasmid (Addgene #42230). A neomycin resistance cassette flanked by two 900 bp homology regions to intron 1 and exon 11 were assembled into the pUC-19 vector as previously described⁵⁶. The Cas9-sgRNA expression plasmids and the homology arm vector were electroporated into 10⁷ VL3-3M2 cells at 340 V for 47 ms in Opti-MEM (Gibco). Neomycin selection was applied after two days. Clonal cells were subsequently generated and screened via PCR using genomic DNA as the template. This involved primers

(Supplementary Table S1) to detect genomicDNA (positive control for WT and KO, gDNA F/R, 800 bp amplicon), primers to verify the presence of the WT allele (mEndoU validation F/R, 1079 bp amplicon), and primers to identify the KO allele (mEndoU validation F/Resistance R, 999 bp amplicon).

mEndoU tagged and mutant constructs

The mEndoU cDNA (NM_001168693) was PCR amplified from VL3-3M2 cDNA with primers containing XhoI (forward) and BglII (reverse) restriction sites and ligated into the pMSCV-PIG or pRL-TK vectors. The Q5 site-directed mutagenesis kit (NEB Cat. E0554S) was used to add a C-terminal FLAG-HA tag, or to create the E285A/H286A catalytically dead mutant version, in pMSCV-PIG.

Viral production and stable integration of mEndoU rescue constructs

VL3-3M2 clonal mEndoU knockout cells were rescued through viral integration of the above EndoU constructs. Plat-E cells were calcium-phosphate transfected with 10 µg of pMSCV-PIG and 2.5 µg VSVG to produce amphotropic VSVG-pseudotyped retrovirus.

RT-qPCR

RNA was extracted from whole cells using ribozol followed by two phenol chloroform extractions (pH 5.2). Superscript II reverse transcriptase was used for cDNA synthesis with 1 µg of total RNA as template. TaqMan probes against mEndoU (NEB Cat. 4351372) were used in the RT-qPCR.

Cell lysis

Cell lysis was carried out by first washing the cells once with PBS buffer and then resuspending them in hypotonic lysis buffer (10 mM Tris-HCl pH 7.5, 10 mM KCl, 5 mM DTT, protease inhibitor). The cells were subsequently incubated on ice for 20 min. Isotonicity was restored by adjusting the KCl concentration to 100 mM using a 5 X supplemental buffer (450 mM KCl, 0.08 U/µl RNaseIN). In certain experiments, lysates were centrifuged at 17,000 × g for 20 min to separate the cytoplasmic fraction and collect the supernatant.

Immunoprecipitations

Immunoprecipitations were carried out using protein A Dynabeads. Beads were prepared by incubation with 16.7 µg/mL anti-mouse Fcγ bridging antibody (Jackson ImmunoResearch AffiniPure Rabbit Anti-Mouse IgG, Fcγ fragment specific, #315-005-008) and 16.7 µg/mL mouse anti-HA.11 antibody (Biolegend, clone 16B12, #901501), sequentially. Cell lysates were incubated with prepared beads for 1 h at room temperature. To equalize the amount of mEndoU across reactions, an excess of cell lysate over bead capacity was used, and saturation of mEndoU binding was verified by western blot.

On-bead mouse mEndoU RNase assays

In a total volume of 10 µL, reactions consisted of (unless used as a variable) 2 mM CaCl₂, 10 mM Tris-HCl (pH 7.5), 100 mM NaCl, 5 µg of total cytoplasmic RNA, or 1 µM of specific RNA oligo (Supplementary Table S2, typically 50 mer 1), and the immunoprecipitated mEndoU. Reactions were incubated at 37 °C, RNA was extracted and run on an 8% urea-PAGE gel, and visualized by SYBR Green II. Densitometry was used to quantify substrate degradation using Quantity One (BioRad). Experiments were done in triplicate from distinct samples.

Production of hEndoU

The open reading frame (ORF) encoding the catalytic domain (135-410) of human EndoU (hEndoU) was sub-cloned into the pET24b(+) plasmid (KanR) downstream of the GB1 protein ORF followed by a hexahistidine tag and a TEV protease cleavage site. Expression of hEndoU was achieved in *Escherichia coli* BL21 Rosetta (DE3) pLysS. The bacteria

were grown in rich LB medium or in M9 minimal medium supplemented with ¹⁵N-labeled NH₄Cl (1 g/L) and ¹³C-labeled glucose (2 g/L) to achieve uniform isotope labeling. The cultures were grown at 37 °C until reaching an OD₆₀₀ of approximately 0.6. Subsequently, protein expression was induced using 0.25 mM IPTG at 15 °C over 16 h. The bacteria were harvested by centrifugation (5000 × g, 10 min, 4 °C), and the resulting pellets were resuspended in ice-cold lysis buffer (20 mM Tris pH 8, 500 mM NaCl, 250 µL/L β-mercaptoethanol). This buffer was further supplemented with 1 mg/mL lysozyme and 10 µL/L DNase I (NEB). Cell lysis was achieved by sonication, running three cycles of 5 min each at 20% amplitude, with 20-s on/off intervals. The lysate was clarified by centrifugation (20,000 × g, 30 min, 4 °C) and the supernatant was loaded onto a gravity-flow histidine affinity chromatography column equilibrated with loading buffer (20 mM Tris pH 8, 500 mM NaCl, 250 µL/L β-mercaptoethanol). The column was washed with 15 mM imidazole (10 CV), and the protein was eluted with 300 mM imidazole (5 CV). The eluted protein was then dialyzed against TEV digestion buffer (10 mM Tris pH 8, 250 mM NaCl, 125 µL/L β-mercaptoethanol) over 16 h, in the presence of His6-TEV protease (1:100 w/w ratio) to digest the GB1-His6 tag. Post-digestion, hEndoU was isolated from the flow-through fraction following its loading onto a gravity-flow histidine affinity chromatography column, and washing with the loading buffer (5 CV). The resulting protein was concentrated, and a large excess of EDTA (250 mM) was added to chelate potential divalent cations. Further purification was achieved using a Superdex 75 column pre-equilibrated with storage buffer (10 mM Tris pH 7, 50 mM NaCl, 1 mM TCEP). Finally, hEndoU was concentrated to a concentration of 500 µM. It was used immediately for enzymatic assays, while it was stored at -80 °C for other experiments. Point mutants were generated using the QuickChange protocol⁵⁷ and hEndoU mutants were purified using the same protocol as the wild type protein. The sequences of the oligonucleotides are given (Supplementary Table S3).

Oligonucleotides synthesis

Oligonucleotides were synthesized using the β-phosphoramidite method with an H8 automated synthesizer (K&A Labs, Germany) on a micromolar scale. For the synthesis of 2'-F RNA analogs, sequences started with a Unylinker solid support (Glen Research), and nucleotides were added sequentially using 2'-F phosphoramidites. For the synthesis of 3' labeled Cyanine 5 RNA, the dye was directly attached to the support, and RNA monomers were used. All phosphoramidites and the Cyanine 5 solid support were purchased from LINK (Scotland). Deprotection of the oligonucleotides was performed according to the suppliers protocols. The concentrated crude oligonucleotides were then resuspended in water. The sample concentration was determined from the absorbance at 260 nm and the molar extinction coefficient of the oligonucleotide. This value was calculated using the Integrated DNA Technology online oligo analyzer tool, which uses the standard nearest neighbor method.

Nuclear magnetic resonance

Nuclear Magnetic Resonance (NMR) spectroscopy was used to analyze protein structure and dynamics. Experiments were performed using either a Bruker AVIII NMR spectrometer at 700 MHz with a room-temperature probe, or a Bruker Avance NEO spectrometer at 800 MHz with a cryogenic 5 mm TCI ¹H-¹³C/¹⁵N/²H Z-gradient probe. These experiments were carried out at 35 °C in a minimal buffer composed of 10 mM Tris (pH 7), 50 mM NaCl, 1 mM TCEP, and 10% D₂O for field frequency lock. We acquired 2D ¹H-¹⁵N and ¹H-¹³C correlation spectra using the SOFAST-HMQC experiment scheme. Sequence-specific backbone assignments of ¹⁵N-¹³C-labeled calcium-activated hEndoU were achieved via classical 3D triple resonance experiments based on the BEST-TROSY principle. The same approach was applied to hEndoU bound to RNA targets. Spectra processing was conducted with Topspin 4 (Bruker) and analyzed

using CARA⁵⁸. Combined ^1H - ^{15}N chemical shift perturbations ($\Delta\delta_{\text{comb}}$) were calculated as $\Delta\delta_{\text{comb}} = \sqrt{\Delta\delta^1\text{H} + 0.14 * \Delta\delta^{15}\text{N}}$, where $\Delta\delta^1\text{H}$ and $\Delta\delta^{15}\text{N}$ are the chemical shift perturbations (in ppm) for ^1H and ^{15}N resonances, respectively. NMR titrations to map the RNA binding surface on calcium-bound hEndoU were performed using a non-cleavable, 2'-F RNA obtained in house via solid-phase synthesis with the following sequence: 5'-AAGUCC-3'.

Structure determination

A sample of the catalytic domain of human hEndoU, spanning residues 135–410, was prepared at a concentration of 12 mg/mL in a buffer containing 10 mM Tris pH 7, 50 mM NaCl, 1 mM TCEP, and 20 mM CaCl₂. The crystallization of hEndoU was carried out at 20 °C using the MCSG4 matrix screen, specifically condition F6, which comprises 0.1 M sodium acetate, 0.1 M HEPES pH 7.5, and 22% PEG 4k. The resulting crystals were flash-frozen in liquid nitrogen using a cryoprotectant solution identical to the crystallization condition but supplemented with 20 % ethylene glycol. Diffraction data were collected at the SOLEIL synchrotron on the PX1 beamline and processed using XDS⁵⁹. Molecular replacement was conducted with Phaser from the Phenix suite⁶⁰, using the AlphaFold 2⁶¹ predicted structure of the hEndoU protein as the model. This process identified two molecules per asymmetric unit, which were subsequently refined using Phenix and BUSTER⁶². Each calcium ion was refined with an occupancy of 100% and exhibited a coordination number of seven. We used the bond-valence method to verify the nature of the coordinated ions, which is suitable given the 1.7 Å resolution of the structure. All coordinated calcium ions showed bond-length distances ranging from 2.16 Å to 2.61 Å, consistent with expected values⁶³. Furthermore, we used the CheckMyMetal webserver to confirm that the geometry of ion coordination corresponded to the expected geometry for calcium coordination⁶⁴. Detailed crystallographic data and refinement statistics are presented in the supplementary materials (Supplementary Table S4).

Enzymatic RNA degradation assays

RNA degradation assays on the human catalytic domain were carried out to assess the relative activity of hEndoU and its mutants. An RNA sequence, 5'-CAGGUUUCCCCAACGGAAAAAA-3', was obtained in-house via solid-phase synthesis. The RNA was labeled at the 3' end with a Cyanine-5 (Cy5) fluorescent probe for detection purposes. In each assay, hEndoU or one of its mutants was prepared at a final concentration of 1 nM in presence of 1 μM of the RNA. The enzymatic reaction was initiated by introducing 2 mM CaCl₂ into the mixture. Samples were collected at 15 time points: 0, 1, 3, 5, 10, 15, 20, 25, 30, 40, 50, 60, 80, 100, and 120 min. The reaction was terminated at each time point with an excess of EDTA to chelate calcium ions in order to prevent hEndoU activation and further RNA degradation. RNA degradation was monitored by resolving the samples on a 16% polyacrylamide gel containing 6 M urea, followed by electrophoresis at 250 V for 50 min. The gel was then scanned with a fluorescence scanner. We used the GelAnalyzer software⁶⁵ to integrate band intensities, which were normalized relative to the zero time point. Each assay was conducted in triplicate to ensure the reproducibility of the results. Measurements were taken from distinct samples for each replicate. Data were processed and analyzed using custom Python scripts. A first-order reaction model, $A * \exp(-k * t)$, was used to fit the enzymatic progress curve, using the *curve_fit* function from the *scipy.optimize* module for regression. The fitted reaction rate k characterizes the activity of each hEndoU mutant. To enable comparison across different mutants, this reaction rate was subsequently expressed in relative terms with respect to the wild-type hEndoU, yielding a dimensionless parameter.

Electrophoretic mobility shift assay

EMSA were conducted to assess the impact of calcium and mutations on RNA binding to EndoU. We prepared 8 % acrylamide/bisacrylamide

(19:1) non-denaturing gels in 0.5 X TBE (44.5 mM Tris base, 44.5 mM boric acid, 1 mM EDTA) supplemented with 5% (v/v) glycerol. Since calcium was used in our assays, we initially attempted to use an EDTA-free 0.5 X TB buffer, but this resulted in inconsistent results, possibly due to trace amounts of heavy metals in the molecular biology-grade glycerol (Sigma-Aldrich G5516) and Tris base (ThermoFisher 17926). Consequently, we used 0.5 X TBE. For the EMSA experiments, samples were prepared in a 20 μL reaction mix with the following buffer composition: 10 mM Tris base (pH 7), 50 mM NaCl, 0.5 mM TCEP. We used a 3'-labeled Cy5 RNA probe containing a single uridylate with the sequence 5'-CACGAGUACCAGAAAACCAAAA-3', at a concentration of 250 nM. To prevent enzymatic degradation of the probe, we used a catalytically inactive hEndoU mutant (H285A), which also served as a background to establish RNA-binding mutants of hEndoU. To assess the impact of calcium on RNA binding, we prepared an equimolar mix of the RNA and hEndoU (H285A), supplemented with increasing concentrations of calcium as follows (mM): 0, 0.1, 0.3, 0.5, 1, 2, 5, 10, 20, 40. To monitor the impact of mutations in hEndoU on RNA-binding activity, we prepared samples containing the RNA probe (250 nM) and calcium ions (2 mM), supplemented with increasing amounts of hEndoU mutant as follows (eq.): 0, 0.25, 0.5, 0.75, 1, 2, 3, 5, 10. For all experiments, 20 μL of loading buffer (50 % glycerol v/v, orange G) were added to each sample prior to loading on the gel. All samples were prepared at room temperature and loaded on the gel immediately upon preparation unless specified otherwise. Electrophoresis was conducted at 100 V for 45 min at room temperature. Each gel was subsequently scanned with a fluorescence scanner. We used GelAnalyzer software⁶⁵ to integrate band intensities to assess the impact of hEndoU mutations on RNA binding. To this end, bands on the lane corresponding to a 1:10 RNA:protein ratio were integrated and expressed as relative fractions of signal for the free RNA, the low molecular weight complex indicating specific binding to uridylate, and the high molecular weight complexes indicating non-specific binding to other bases.

Molecular dynamics

Molecular dynamics simulations were performed using the GROMACS software package⁶⁶ (version 2022.1). System preparation was achieved through CHARMM-GUI and the Input Generator module⁶⁷, which was also used to apply single amino-acid substitutions for hEndoU mutants. To monitor the stability of the calcium binding sites, we used the crystal structure of hEndoU bound to calcium ions as input. To monitor the binding of calcium to apo-hEndoU, we removed calcium ions from the crystal structure and used the resulting structure as input. Calcium ions were then reintroduced into the system as salt ions, and simulations were run in triplicate. Calcium binding events to hEndoU were consistently detected across the replicates. To propose an ensemble of models of calcium-activated hEndoU in complex with RNA, we used the AlphaFold (AF) 3³⁸ webserver with the human hEndoU sequence (135–410), a (U)6 RNA, and four calcium ions as inputs. The top ranked model accurately reproduced each of the calcium binding sites, with an RMSD of 0.313 Å between the crystal structure of calcium-activated hEndoU and the corresponding part of the AF3 model. Therefore, we created a hybrid model comprising the experimental structure of calcium activated hEndoU in complex with the AF3-modeled bound RNA. This resulting model was used as input for MD simulations and structures were clustered over the trajectory based on RNA conformations. The coordinates of the structural model can be obtained from S.C. upon request. For all simulations, we used the CHARMM36m force field and the TIP3P water model. Each system was solvated in a cubic box with a 1.0 nm buffer zone between the protein and the box edge, and 50 mM NaCl was added with adjustments to neutralize the system. After downloading the generated inputs, energy minimization was executed in GROMACS using the steepest descent algorithm until the maximum force was below

1000 kJ/mol/nm, and then equilibration was done under NVT conditions for 125 ps. Particle Mesh Ewald was used for long-range electrostatics, with a cutoff of 1.0 nm for van der Waals interactions, and a time step of 2 fs was applied. The production phase of the simulations was carried out for 1 μs under NPT conditions at a temperature of 35 °C and a pressure of 1 bar. The output was then analyzed for various parameters using the built-in tools of GROMACS.

SEC-SAXS experiments

SEC-SAXS experiments were conducted on the SWING beamline at the SOLEIL synchrotron (Saint-Aubin, France). All procedures were carried out at a temperature of 35 °C using a buffer composed of 10 mM Tris pH 7, 50 mM NaCl, and 1 mM TCEP. hEndoU was prepared to a concentration of 500 μM. A volume of 75 μL was injected onto a size exclusion column (Bio-SEC 3 Agilent 100 Å), and was then eluted directly into the SAXS flow-through capillary cell at a flow rate of 0.3 mL/min. SAXS data were collected using an EigerX 4 M detector situated 2 m away, using the definition of the momentum transfer q : $q = 4\pi \sin(\theta)/\lambda$, where 2θ represents the scattering angle and λ the X-ray wavelength (1.033 Å for these experiments). The overall SEC-SAXS setup has been described in earlier publications⁶⁸. A total of 900 SAXS frames were continuously recorded during elution, each with a duration of 1.99 s and a 0.01 s dead time between frames. 180 frames were collected before the dead volume to account for buffer scattering. Data reduction to absolute units, buffer subtraction, and averaging of identical frames corresponding to the elution peak were performed using the in-house SWING software FOXTROT⁶⁹ and BioXTAS⁷⁰. BioXTAS was also used to compute the gyration ratio and to estimate the molecular weight based on the volume of correlation. The fitting of the hEndoU homology model to the experimental SAXS data were accomplished through the Crysolv software, part of the ATSAS Suite⁷¹. Essential Small Angle Scattering (SAS) details are provided in the supplementary material (Supplementary Table S5).

Intrinsic fluorescence

To assess the impact of calcium binding on the tertiary structure of hEndoU, we measured the intrinsic fluorescence of the protein with a temperature-controlled spectrofluorometer (FS5, Edinburgh Instruments). Protein samples were prepared at 10 μM in a buffer of 10 mM Tris pH 7, 50 mM NaCl, and 1 mM TCEP, and their fluorescence emission spectra were recorded at 35 °C. Emissions from 300 to 525 nm were recorded to detect fluorescence from tryptophan, tyrosine, and phenylalanine. Slit widths for excitation and emission were set at 5 nm, and each spectrum was an average of three scans, corrected for buffer baseline.

Statistical tests and procedures

Statistical tests and procedures were performed using in-house python scripts, relying on widely recognized *scipy* and *statsmodels* libraries. Comparison between groups of data was achieved through pairwise t-tests (*scipy.stats.ttest_ind*), ensuring data normality (*scipy.stats.shapiro*) and variance homogeneity (*scipy.stats.levene*). Computed *p*-values were adjusted for multiple comparisons using the Benjamini/Hochberg method (*statsmodels.stats.multitest.multipletests*). Comparison between parameters with associated errors was achieved through as follows: z-scores were calculated pairwise as the difference between parameters divided by the standard error of the difference. Two-tailed *p*-values were then computed from the z-score using a normal distribution survival function (*scipy.stats.norm.sf*). Resulting *p*-values were adjusted for multiple comparisons using the Bonferroni correction method (*statsmodels.stats.multitest.multipletests*).

Data availability

The data supporting the findings of this study are available from the corresponding authors upon request. The atomic coordinates of the

calcium-activated hEndoU structure have been deposited in the PDB under the accession code **9FTW**. The chemical shift assignments for calcium-activated hEndoU have been deposited to the BMRB with accession code **52564**³⁷. Source data are provided with this paper. Through this work, we also referred to the following PDB accession numbers: **2CIW**, **6RSA**, **7TJ2**, **5HKQ**, **7RBO**, and **1U1B**. Source data are provided with this paper.

References

1. Kushner, S. R. mRNA Decay in Prokaryotes and Eukaryotes: Different Approaches to a Similar Problem. *IUBMB Life* **56**, 585–594 (2004).
2. Evgenieva-Hackenberg, E. & Klug, G. RNA Degradation in Archaea and Gram-Negative Bacteria Different from Escherichia coli. *Prog. Mol. Biol. Transl. Sci.* **85**, 275–317 (2009).
3. Schmid, M. & Jensen, T. H. The exosome: a multipurpose RNA-decay machine. *Trends Biochem. Sci.* **33**, 501–510 (2008).
4. Tomecki, R. & Dziembowski, A. Novel endoribonucleases as central players in various pathways of eukaryotic RNA metabolism. *RNA* **16**, 1692–1724 (2010).
5. Paysan-Lafosse, T. et al. InterPro in 2022. *Nucleic Acids Res.* **51**, D418–D427 (2023).
6. Mushegian, A., Sorokina, I., Eroshkin, A. & Dlakić, M. An ancient evolutionary connection between Ribonuclease A and EndoU families. *RNA* **26**, 803–813 (2020).
7. Raines, R. T. Ribonuclease A. *Chem. Rev.* **98**, 1045–1066 (1998).
8. Smyth, D. G., Stein, W. H. & Moore, S. The sequence of amino acid residues in bovine pancreatic ribonuclease: revisions and confirmations. *J. Biol. Chem.* **238**, 227–34 (1963).
9. Findlay, D., Herries, D., Mathias, A., Rabin, B. & Ross, C. The active site and mechanism of action of bovine pancreatic ribonuclease. 7. The catalytic mechanism. *Biochemical J.* **85**, 152–153 (1962).
10. AVEY, H. P. et al. Structure of Ribonuclease. *Nature* **213**, 557–562 (1967).
11. Michalska, K. et al. Functional plasticity of antibacterial EndoU toxins. *Mol. Microbiol.* **109**, 509–527 (2018).
12. Caffarelli, E., Maggi, L., Fatica, A., Jiricny, J. & Bozzoni, I. A Novel Mn⁺-Dependent Ribonuclease That Functions in U16 SnoRNA Processing in *X. laevis*. *Biochem. Biophys. Res. Commun.* **233**, 514–517 (1997).
13. Gioia, U. et al. Functional Characterization of XendoU, the Endoribonuclease Involved in Small Nucleolar RNA Biosynthesis. *J. Biol. Chem.* **280**, 18996–19002 (2005).
14. Laneve, P. et al. Purification, Cloning, and Characterization of XendoU, a Novel Endoribonuclease Involved in Processing of Intron-encoded Small Nucleolar RNAs in *Xenopus laevis*. *J. Biol. Chem.* **278**, 13026–13032 (2003).
15. Mistry, J. et al. Pfam: The protein families database in 2021. *Nucleic Acids Res.* **49**, D412–D419 (2021).
16. Bohn, H. & Winckler, W. Isolierung und Charakterisierung eines neuen Plazenta-Gewebsproteins (PP11). *Arch. Gynecol.* **229**, 293–301 (1980).
17. Laneve, P. et al. The Tumor Marker Human Placental Protein 11 Is an Endoribonuclease. *J. Biol. Chem.* **283**, 34712–34719 (2008).
18. Xu, C. et al. Integrated Analysis Reveals ENDOU as a Biomarker in Head and Neck Squamous Cell Carcinoma Progression. *Front. Oncol.* **10**, 522332 (2021).
19. Basic, V., Zhang, B., Domert, J., Pellas, U. & Tot, T. Integrative meta-analysis of gene expression profiles identifies FEN1 and ENDOU as potential diagnostic biomarkers for cervical squamous cell carcinoma. *Oncol. Lett.* **22**, 840 (2021).
20. Lou, Y., Ren, L. & Wang, L. Hsa_circ_0049396 inhibited oral squamous cell carcinoma progression by regulating the miR-663b/ENDOU axis. *Genomics* **115**, 110553 (2023).
21. Inaba, N. et al. Immunohistochemical detection of pregnancy-specific protein (SP1) and placenta-specific tissue proteins (PP5,

- PP10, PP11 and PP12) in ovarian adenocarcinomas. *Oncodev. Biol. Med.* **3**, 379–89 (1982).
22. Inaba, N., Renk, T., Wurster, K., Rapp, W. & Bohn, H. Ectopic synthesis of pregnancy specific beta 1-glycoprotein (SP1) and placental specific tissue proteins (PP5, PP10, PP11, PP12) in non-trophoblastic malignant tumours possible markers in oncology. *Klin. Wochenschr.* **58**, 789–791 (1980).
 23. Schwarz, D. S. & Blower, M. D. The calcium-dependent ribonuclease XendoU promotes ER network formation through local RNA degradation. *J. Cell Biol.* **207**, 41–57 (2014).
 24. Zhao, G. & Blackstone, C. ER Morphology: Sculpting with XendoU. *Curr. Biol.* **24**, R1170–R1172 (2014).
 25. Poe, J. C. et al. EndoU is a novel regulator of AICD during peripheral B cell selection. *J. Exp. Med.* **211**, 57–69 (2014).
 26. Laneve, P. et al. Drosophila CG3303 is an essential endoribonuclease linked to TDP-43-mediated neurodegeneration. *Sci. Rep.* **7**, 41559 (2017).
 27. Ujisawa, T. et al. Endoribonuclease ENDU-2 regulates multiple traits including cold tolerance via cell autonomous and nonautonomous controls in *Caenorhabditis elegans*. *Proc. Natl Acad. Sci.* **115**, 8823–8828 (2018).
 28. Zhang, D., de Souza, R. F., Anantharaman, V., Iyer, L. M. & Aravind, L. Polymorphic toxin systems: Comprehensive characterization of trafficking modes, processing, mechanisms of action, immunity and ecology using comparative genomics. *Biol. Direct* **7**, 18 (2012).
 29. Nedialkova, D. D. et al. Biochemical Characterization of Arterivirus Nonstructural Protein 11 Reveals the Nidovirus-Wide Conservation of a Replicative Endoribonuclease. *J. Virol.* **83**, 5671–5682 (2009).
 30. Bhardwaj, K., Guarino, L. & Kao, C. C. The Severe Acute Respiratory Syndrome Coronavirus Nsp15 Protein Is an Endoribonuclease That Prefers Manganese as a Cofactor. *J. Virol.* **78**, 12218–12224 (2004).
 31. Renzi, F. et al. The structure of the endoribonuclease XendoU: From small nucleolar RNA processing to severe acute respiratory syndrome coronavirus replication. *Proc. Natl Acad. Sci.* **103**, 12365–12370 (2006).
 32. Heng, T. S. P. et al. The Immunological Genome Project: networks of gene expression in immune cells. *Nat. Immunol.* **9**, 1091–1094 (2008).
 33. Uhlen, M. et al. Tissue-based map of the human proteome. *Science* **347**, 1260419 (2015).
 34. Groves, T. et al. In vitro maturation of clonal CD4+CD8+ cell lines in response to TCR engagement. *J. Immunol.* **154**, 5011–22 (1995).
 35. Waterhouse, A. et al. SWISS-MODEL: homology modelling of protein structures and complexes. *Nucleic Acids Res.* **46**, W296–W303 (2018).
 36. Svergun, D., Barberato, C. & Koch, M. H. J. CRYSTOL – a Program to Evaluate X-ray Solution Scattering of Biological Macromolecules from Atomic Coordinates. *J. Appl. Crystallogr.* **28**, 768–773 (1995).
 37. Malard, F., Karginov, F. V. & Campagne, S. 1H, 13C and 15N backbone resonance assignment of the calcium-activated EndoU endoribonuclease. *Biomol. NMR Assign.* **18**, 263–267 (2024).
 38. Abramson, J. et al. Addendum: Accurate structure prediction of biomolecular interactions with AlphaFold 3. *Nature* **636**, E4–E4 (2024).
 39. Yang, W., Lee, J. Y. & Nowotny, M. Making and Breaking Nucleic Acids: Two-Mg²⁺-Ion Catalysis and Substrate Specificity. *Mol. Cell* **22**, 5–13 (2006).
 40. Cuchillo, C. M. et al. The role of 2', 3'-cyclic phosphodiesters in the bovine pancreatic ribonuclease A catalysed cleavage of RNA: intermediates or products? *FEBS Lett.* **333**, 207–210 (1993).
 41. Qi, W. et al. The secreted endoribonuclease ENDU-2 from the soma protects germline immortality in *C. elegans*. *Nat. Commun.* **12**, 1262 (2021).
 42. Keen, C. L., Uriu-Adams, J. Y., Ensunsaa, J. L. & Gershwin, M. E. Trace Elements/Minerals and Immunity. In: *Handbook of Nutrition and Immunity* 117–140 (Humana Press, 2004) https://doi.org/10.1007/978-1-59259-790-1_6.
 43. Jenne, D. & Stanley, K. K. Nucleotide sequence and organization of the human S-protein gene: repeating peptide motifs in the ‘peixin’ family and a model for their evolution. *Biochemistry* **26**, 6735–6742 (1987).
 44. Alquraini, A. et al. The interaction of lubricin/proteoglycan 4 (PRG4) with toll-like receptors 2 and 4: an anti-inflammatory role of PRG4 in synovial fluid. *Arthritis Res. Ther.* **17**, 353 (2015).
 45. Goding, J. W., Grobben, B. & Slegers, H. Physiological and pathophysiological functions of the ecto-nucleotide pyrophosphatase/phosphodiesterase family. *Biochim. Biophys. Acta Mol. Basis Dis.* **1638**, 1–19 (2003).
 46. Droujinine, I. A. et al. Proteomics of protein trafficking by in vivo tissue-specific labeling. *Nat. Commun.* **12**, 2382 (2021).
 47. Bootman, M. D. & Bultynck, G. Fundamentals of Cellular Calcium Signaling: A Primer. *Cold Spring Harb. Perspect. Biol.* **12**, a038802 (2020).
 48. Pillon, M. C. et al. Cryo-EM structures of the SARS-CoV-2 endoribonuclease Nsp15 reveal insight into nuclease specificity and dynamics. *Nat. Commun.* **12**, 636 (2021).
 49. Huang, T. et al. Kinetic analysis of RNA cleavage by coronavirus Nsp15 endonuclease: Evidence for acid–base catalysis and substrate-dependent metal ion activation. *J. Biol. Chem.* **299**, 104787 (2023).
 50. Wang, X. & Zhu, B. SARS-CoV-2 nsp15 preferentially degrades AU-rich dsRNA via its dsRNA nickase activity. *Nucleic Acids Res.* **52**, 5257–5272 (2024).
 51. Bhardwaj, K., Sun, J., Holzenburg, A., Guarino, L. A. & Kao, C. C. RNA Recognition and Cleavage by the SARS Coronavirus Endoribonuclease. *J. Mol. Biol.* **361**, 243–256 (2006).
 52. Frazier, M. N. et al. Characterization of SARS2 Nsp15 nuclease activity reveals it's mad about U. *Nucleic Acids Res.* **49**, 10136–10149 (2021).
 53. Kim, Y. et al. Tipiracil binds to uridine site and inhibits Nsp15 endoribonuclease NendoU from SARS-CoV-2. *Commun. Biol.* **4**, 193 (2021).
 54. Ivanov, K. A. et al. Major genetic marker of nidoviruses encodes a replicative endoribonuclease. *Proc. Natl Acad. Sci.* **101**, 12694–12699 (2004).
 55. Jamet, A. et al. A New Family of Secreted Toxins in Pathogenic Neisseria Species. *PLoS Pathog.* **11**, e1004592 (2015).
 56. Sternburg, E. L., Dias, K. C. & Karginov, F. V. Selection-dependent and Independent Generation of CRISPR/Cas9-mediated Gene Knockouts in Mammalian Cells. *J. Vis. Exper.* <https://doi.org/10.3791/55903> (2017).
 57. Liu, H. & Naismith, J. H. An efficient one-step site-directed deletion, insertion, single and multiple-site plasmid mutagenesis protocol. *BMC Biotechnol.* **8**, 91 (2008).
 58. Keller, R. *The Comptuer-Aided Resonance Assignment Tutorial* (Cantina Verlag, 2004).
 59. Kabsch, W. XDS. *Acta Crystallogr D. Biol. Crystallogr* **66**, 125–132 (2010).
 60. Liebschner, D. et al. Macromolecular structure determination using X-rays, neutrons and electrons: recent developments in Phenix. *Acta Crystallogr D. Struct. Biol.* **75**, 861–877 (2019).
 61. Jumper, J. et al. Highly accurate protein structure prediction with AlphaFold. *Nature* **596**, 583–589 (2021).
 62. Bricogne G., et al. BUSTER version 2.10.4 (Global Phasing Ltd, 2017).
 63. Müller, P., Köpke, S. & Sheldrick, G. M. Is the bond-valence method able to identify metal atoms in protein structures? *Acta Crystallogr D. Biol. Crystallogr* **59**, 32–37 (2003).
 64. Zheng, H. et al. CheckMyMetal: a macromolecular metal-binding validation tool. *Acta Crystallogr D. Struct. Biol.* **73**, 223–233 (2017).

65. Lazar, I. & Lazar, I. GelAnalyzer 23.1.1. available at www.gelanalyzer.com.
66. Van Der Spoel, D. et al. GROMACS: Fast, flexible, and free. *J. Comput Chem.* **26**, 1701–1718 (2005).
67. Lee, J. et al. CHARMM-GUI Input Generator for NAMD, GROMACS, AMBER, OpenMM, and CHARMM/OpenMM Simulations Using the CHARMM36 Additive Force Field. *J. Chem. Theory Comput.* **12**, 405–413 (2016).
68. Thureau, A., Roblin, P. & Pérez, J. BioSAXS on the SWING beamline at Synchrotron SOLEIL. *J. Appl. Crystallogr.* **54**, 1698–1710 (2021).
69. David, G. & Pérez, J. Combined sampler robot and high-performance liquid chromatography: a fully automated system for biological small-angle X-ray scattering experiments at the Synchrotron SOLEIL SWING beamline. *J. Appl. Crystallogr.* **42**, 892–900 (2009).
70. Hopkins, J. B., Gillilan, R. E. & Skou, S. BioXTAS RAW: improvements to a free open-source program for small-angle X-ray scattering data reduction and analysis. *J. Appl. Crystallogr.* **50**, 1545–1553 (2017).
71. Franke, D. et al. ATSAS 2.8: a comprehensive data analysis suite for small-angle scattering from macromolecular solutions. *J. Appl. Crystallogr.* **50**, 1212–1225 (2017).

Acknowledgements

We would like to thank Stephen Smale for sharing the VL3-3M2 cell line, and the Zhang lab for sharing the pX330 plasmid. This work is funded in part by NIH grant 1R01GM152548 (to F.V.K. and S.C.). We thank INSERM and CNRS for funding. We are grateful to Dr. Mikayel Aznauryan for providing us with access to the fluorescence spectroscopy facilities. We thank INSERM for funding through the ARNA internal call (to S.C., S.F. and P.B.). We acknowledge SOLEIL for provision of synchrotron radiation facilities and we would like to thank PX1 staff members for assistance in using beamline PX1. We would like to thank Dr. Aurélien Thureau from SWING beamline at SOLEIL for assistance during SAXS data collection.

Author contributions

S.C., F.V.K., S.F., and F.M. designed the research. P.B. and B.V. synthesized the RNAs and 2'F analogs used in the study. K.D. and F.V.K. performed experiments on the mouse thymic lymphoma cell line VL3-3M2, including CRISPR/Cas9 knockout of EndoU and biochemical characterization of both endogenous and immunoprecipitated EndoU. F.M. and S.T. performed crystallogenesis. S.F. performed freezing and structure determination. S.T. performed crystallographic data collection. F.M. and S.C. conducted NMR spectroscopy studies. F.M. and M.B. carried out RNA degradation assays with recombinant EndoU. F.M.

conducted EMSA experiments, SEC-SAXS experiments, AlphaFold modeling, and MD simulations. F.M. and F.V.K. wrote the initial draft of the manuscript. F.M., S.C., F.V.K., S.F., and S.T. discussed the initial draft and contributed to the final version of the manuscript.

Competing interests

The authors declare no competing interests.

Additional information

Supplementary information The online version contains supplementary material available at <https://doi.org/10.1038/s41467-025-58462-6>.

Correspondence and requests for materials should be addressed to Sébastien Fribourg, Fedor V. Karginov or Sébastien Campagne.

Peer review information *Nature Communications* thanks Kozo Tomita and the other, anonymous, reviewers for their contribution to the peer review of this work. A peer review file is available

Reprints and permissions information is available at <http://www.nature.com/reprints>

Publisher's note Springer Nature remains neutral with regard to jurisdictional claims in published maps and institutional affiliations.

Open Access This article is licensed under a Creative Commons Attribution-NonCommercial-NoDerivatives 4.0 International License, which permits any non-commercial use, sharing, distribution and reproduction in any medium or format, as long as you give appropriate credit to the original author(s) and the source, provide a link to the Creative Commons licence, and indicate if you modified the licensed material. You do not have permission under this licence to share adapted material derived from this article or parts of it. The images or other third party material in this article are included in the article's Creative Commons licence, unless indicated otherwise in a credit line to the material. If material is not included in the article's Creative Commons licence and your intended use is not permitted by statutory regulation or exceeds the permitted use, you will need to obtain permission directly from the copyright holder. To view a copy of this licence, visit <http://creativecommons.org/licenses/by-nc-nd/4.0/>.

© The Author(s) 2025